# Identifying, Tracking, and Evaluating Mechanisms of North American Cold Air Outbreaks (CAOs) Using a Feature Tracking Approach

JACK STONE,[a] MELISSA GERVAIS,[a,b] KEVIN A. BOWLEY,[a] AND COLIN ZARZYCKI[a]

[a] *Department of Meteorology and Atmospheric Science, The Pennsylvania State University, University Park, Pennsylvania*
[b] *Institute for Computational and Data Sciences, The Pennsylvania State University, University Park, Pennsylvania*

(Manuscript received 27 November 2023, in final form 12 November 2024, accepted 11 December 2024)

ABSTRACT: North American cold air outbreaks (CAOs) are large-scale temperature extremes that typically originate in the high latitudes and impact the midlatitudes in winter. As they transit southward, they can have significant socioeconomic consequences. CAOs from winter (DJF) 1979 to 2020 were identified in the fifth major global reanalysis produced by the European Centre for Medium-Range Weather Forecasts (ERA5) using an automated feature tracking approach (TempestExtremesV2.1). This allowed for the systematic identification of a large number of cases without using predetermined, Eulerian regions. Another important advantage of this approach was the ability to compute a feature tracked thermodynamic energy budget in a nonfixed domain for every identified CAO event. As an example, the thermodynamic energy budget analysis was used to quantify important processes for the 18–23 January 1985 CAO. The dominant mechanisms of cooling and warming as well as lysis locations (i.e., eastern or western) were then used to generalize detected CAO events into subcategories. The associated statistics, spatial footprints, and composites of 500-hPa height, sea level pressure, and temperature and winds at 850 hPa were analyzed for three subcategories that contained the majority of events. This analysis revealed that CAO events that form and dissipate through different mechanisms occur in different regions, have different intensities, and are associated with different large-scale circulation patterns. Finally, the analysis of associated North Atlantic Oscillation (NAO) and Pacific–North American (PNA) teleconnection pattern revealed that the PNA is typically in a positive phase for eastern CAO events and in a negative phase for western events resulting primarily from horizontal advection, whereas the NAO did not have any significant relationship.

KEYWORDS: Atmosphere; North America; Cold air surges; Extreme events; Thermodynamics

## 1. Introduction

Continental cold air outbreaks (CAOs), or alternatively cold spells (Messori et al. 2016; Matthias and Kretschmer 2020; Messori and Faranda 2023), are persistent negative temperature extremes that can last from several days to weeks (e.g., Walsh et al. 2001; Cellitti et al. 2006; Smith and Sheridan 2020; Millin et al. 2022). They can have devastating socioeconomic impacts, with extreme CAOs resulting on average in 30 deaths per year (Cellitti et al. 2006) and billions of dollars in crop damage and livestock death (Rogers and Rohli 1991), as well as transportation delays and damaged infrastructure (Screen et al. 2015). Duration and timing of CAOs can be just as impactful as intensity. For example, in April 2007, an extreme CAO affecting much of the United States led to two billion U.S. dollars in agricultural losses because it occurred after most crops had begun to bloom (Gu et al. 2008). Likewise, the deaths, economic loss, and infrastructural damage from an extreme February 2021 CAO in the central and southern United States were largely due to the long duration and lack of preparedness, rather than intensity alone (Bolinger et al. 2022).

Cold air masses are typically associated with near-surface temperature inversions caused by radiative cooling over highly emissive surfaces like snow (Curry 1983; Tanaka and Milkovich 1990). Unlike earlier classical depictions of cold airmass formation as extremely shallow surface formations (Wexler 1936), Turner and Gyakum (2011) proposed a multistage formation process in northwest Canada, where the entirety of the 1000–500-hPa layer of the troposphere cools and diabatic processes like ice crystal radiation and sublimation are important. Turner and Gyakum (2011) also note that the final stage of cold airmass formation in northwest Canada is commonly associated with cold air damming and an anticyclone to the leeward side of the Rocky Mountains. Cold air damming can intensify cold air masses to the lee of the Appalachians (Bell and Bosart 1988; Bailey et al. 2003; Rackley and Knox 2016; Dunn 1987; Colle and Mass 1995; Turner and Gyakum 2011) in North America. It is most easily achieved when the air mass to the lee of the mountain barrier is statically stable, which is the case with a shallow cold-core anticyclone situated under an inversion (Dunn 1987). Thus, cold air damming onset is often concurrent with an anticyclone positioned to the north of the damming region (Dunn 1987; Bell and Bosart 1988; Bailey et al. 2003). Diabatic processes like evaporative cooling can also increase the static stability of the cold air mass (Bailey et al. 2003). As the aptly named "cold dome" develops, strong cold air advection at the surface is contrasted with warm air advection aloft, which strengthens the aforementioned inversion (Bell and Bosart 1988). Typically, the resulting force balance manifests as a strong low-level barrier jet surging south alongside the topography (Bell and Bosart 1988; Colle and Mass 1995).

Denotes content that is immediately available upon publication as open access.

*Corresponding author*: Jack Stone, jzs7008@psu.edu

DOI: 10.1175/MWR-D-23-0265.1

The genesis of North American CAOs often occurs in Alaska or northwest Canada, before they transit into the midlatitudes in the form of a cold anticyclone (Dallavalle and Bosart 1975; Colle and Mass 1995; Colucci et al. 1999; Walsh et al. 2001; Turner et al. 2013). In particular, Walsh et al. (2001) found that CAOs that impact the eastern United States and Gulf Coast region often occur when pools of cold air break off of cold air masses at higher latitudes. In contrast, CAOs that impact the Midwest United States often occur through cold air advection on the eastern side of stationary cold air masses that remain further north (Walsh et al. 2001). Iwasaki et al. (2014) used isentropic analysis to identify Lagrangian mean transports of cold air masses via two dominant pathways (one being into North America through the Hudson Bay and the other through Eurasia). They also found that these mean airmass pathways are consistent with CAOs occurring in eastern North America based on climatologies in other studies (Iwasaki et al. 2014). While CAOs are often discussed in conjunction with cold air masses, in this study, we use the term "cold air mass" to describe any large-scale region of extreme cold temperatures, whereas "cold air outbreak" will be used specifically to describe events where a cold air mass is sustained for at least 3 days and impacts the midlatitudes.

Dynamic forcing for CAOs includes upper-level ridging and associated horizontal convergence that can lead to the initial pressure rises associated with a cold anticyclone (Dallavalle and Bosart 1975). Millin et al. (2022) found two dominant regimes associated with CAOs in the Midwest, based on a sample of events from 1950 to 2021: anomalous ridging over Alaska and anomalous ridging over the entire Arctic. Similarly, positive sea level pressure anomalies over the Alaska–Yukon border (Walsh et al. 2001) along with the coupling of an upper-level ridge over the Arctic with an upper-level trough over the Great Lakes have been identified as a precursor to CAOs (Konrad 1996). Biernat et al. (2021) also noted that the amplification of an upper-level ridge situated over the North Pacific or western North America could contribute to the equatorward transport of CAO cold pools. Messori et al. (2016) found that the large-scale circulation preceding North American CAOs involved advection from the Arctic, and a zonal and southerly shifted North Atlantic jet. Grotjahn et al. (2016) identified common precursors to be surface cyclogenesis over the eastern United States, low 500-hPa geopotential heights over the Great Lakes region, and southeastward movement of an upper-level shortwave from western Canada. When comparing the behavior of two different composites of cold anticyclones, Dallavalle and Bosart (1975) observed that if a trough downstream of an intensifying ridge centered on northwestern Canada is established aloft, it can result in uninterrupted northwesterly flow transiting cold air toward the Gulf of Mexico. In the absence of this flow, the anticyclone would remain stationary until such upper-level flow is initiated. Once the cold air moves southward, the CAO and/or associated anticyclone–cyclone couplet may either undergo lysis due to processes such as subsidence and surface heating or reintensify (Dallavalle and Bosart 1975; Konrad and Colucci 1989; Colucci et al. 1999).

In terms of associations with known teleconnection patterns, a negative North Atlantic Oscillation (NAO) has been shown to precede cold anomalies in the eastern United States (Walsh et al. 2001; Cellitti et al. 2006; Westby et al. 2013; Grotjahn et al. 2016), while a negative (positive) Pacific–North American (PNA) teleconnection pattern leads to cold anomalies in the northwest (southeast) (Leathers et al. 1991; Rogers and Rohli 1991; Westby et al. 2013; Grotjahn et al. 2016; Messori et al. 2016). The mechanism by which the PNA leads to these cold anomalies is well understood; the enhanced ridge over northwestern North America coupled with the enhanced trough over the southeast United States characteristic of the positive phase of the PNA allows for cold air to travel south more readily (Leathers et al. 1991).

A common method for studying CAOs is to analyze one or more case studies individually (Colucci et al. 1999; Ackerman et al. 2005; Bolinger et al. 2022) or composite multiple case studies (Dallavalle and Bosart 1975; Colle and Mass 1995). The advantages of case studies include the ability to analyze specific antecedent conditions, account for the event transiting through multiple regions, capture the full development of the event through time, and conduct a detailed analysis of the dynamic and thermodynamic processes. However, bias in the selection of cases (typically focusing on the most well-known or extreme events) and small sample sizes make it difficult to generalize CAOs. Computing composites of these case studies can help overcome some of the difficulty generalizing processes from a single case (Grotjahn et al. 2016); however, they can still be subject to the same biases in the event classification.

Many studies instead implement Eulerian approaches to identify and analyze CAOs, which has the advantage of capturing a complete set of cases (Walsh et al. 2001; Portis et al. 2006; Vavrus et al. 2006; Turner and Gyakum 2011; Turner et al. 2013; Westby et al. 2013; Ayarzagüena and Screen 2016; Grotjahn and Zhang 2017; Smith and Sheridan 2020; Millin et al. 2022). This often involves averaging temperature anomalies in fixed regions and applying criteria for duration, intensity, and synoptic independence (e.g., Millin et al. 2022). The Eulerian approach allows for identification of a larger sample of events, a flexible and easily changeable definition of criteria, and computational efficiency. However, CAOs cover large, constantly changing areas that are difficult to capture when using fixed, predetermined regions. Several studies have implemented Lagrangian/kinematic back trajectories using the three-dimensional wind field subsequently to event identification for continental (Walsh et al. 2001; Grotjahn and Zhang 2017; Hartig et al. 2023) or marine (Papritz and Spengler 2017) CAOs. Lagrangian back trajectories are advantageous in that they allow for insight into the origin of parcels of cold air, evolution of features through time, and quantification of meteorological quantities throughout the life cycle of events (Papritz and Spengler 2017).

Once a CAO has been identified, thermodynamic energy budgets can be a useful tool for identifying the processes driving CAO genesis, intensification, and lysis. Several studies have quantified and tracked thermodynamic processes in a fixed domain using a region centered on a moving CAO (Tanaka and Milkovich 1990; Konrad and Colucci 1989;

Colucci et al. 1999). However, computing a thermodynamic energy budget in a fixed domain does not allow for a full picture of a CAO's size, shape, and how it interacts with dynamic fields, even if that fixed domain moves with its center. Furthermore, thermodynamic processes may be spatially heterogeneous, in that one term can warm or cool in different parts of the CAO. This in turn can mask the importance of their role when averaging over a fixed domain. In contrast, Papritz and Spengler (2017) analyzed the Lagrangian thermodynamic evolution of air parcels in marine CAOs with nonfixed domains using kinematic back trajectories.

The goal of this study is to explore the dynamic and thermodynamic mechanisms impacting transiting North American continental cold air outbreaks using a new feature tracked repository of CAO cases. Automated feature tracking algorithms can circumvent many of the issues associated with CAO event identification and analysis identified above, while providing many of the same advantages of Lagrangian back trajectories. In this study, we use TempestExtremesV2.1 (TE), a feature tracking algorithm, to identify and track winter CAOs from 1979 to 2020. This methodology can capture a larger number of CAO events, while considering the full spatial and temporal extent of events, and without relying on predetermined study regions. Furthermore, automated feature tracking allowed for the computation of a feature tracked thermodynamic energy budget in a nonfixed domain. To provide an example, results from this tracking method and thermodynamic energy budget calculations are shown for the 18–23 January 1985 CAO, previously analyzed in Colucci et al. (1999). Statistics of all identified CAO events are computed including the number of events per year, intensity, and duration. Last, all detected CAOs are generalized by the dominant mechanisms of warming and cooling in order to quantify the relative importance of these processes.

## 2. Data and methods

### a. Data

Hourly data at 0.25° horizontal grid spacing were obtained from the fifth major global reanalysis produced by the European Centre for Medium-Range Weather Forecasts (ECMWF) [ERA5; Hersbach et al. (2020)]. We limited our analysis to the winter season [December–February (DJF)] from 1979–80 (i.e., 1979) to 2020–21 (i.e., 2020). Daily indices of the NAO and PNA teleconnection pattern for the same winter seasons were obtained from the National Oceanic and Atmospheric Administration (NOAA) Climate Prediction Center (CPC). These indices are computed as the first and second rotated principal components of 500-hPa height anomalies in the Northern Hemisphere as in Barnston and Livezey (1987).

### b. CAO event identification

We applied TE, a feature detection, tracking, and analysis framework developed by Ullrich and Zarzycki (2017) for either traditional grids (such as for the ERA5) or unstructured grids. One advantage of using TE is that it captures information about changes in spatial extent and location of events as in case studies, but can be automated to analyze large amounts of climate data, as in most Eulerian methodologies. The algorithm has been applied successfully to track tropical and extratropical cyclones (Chavas et al. 2017; Balaguru et al. 2020; Roberts et al. 2020), atmospheric rivers (McClenny et al. 2020; Patricola et al. 2020; Zhou et al. 2021), and other atmospheric phenomena (Pinheiro et al. 2019; You and Ting 2021), but this was the first application of the feature tracking algorithm to identify cold air masses.

TempestExtremes implements several core algorithms (kernels) that can be combined or run one at a time for nodal (pointwise) and areal feature tracking. The two kernels of TE that provided the basis of cold air mass identification and tracking in this study were DetectBlobs and StitchBlobs. DetectBlobs was used for the identification of areal features. Candidate regions were selected for each time slice based on an input threshold of a given atmospheric variable (here daily averaged 2-m temperature standardized anomalies) and then marked using a binary mask (Ullrich et al. 2021). StitchBlobs was used to track areal features in time, assigning connected features a unique ID and then applying criteria for overlap and minimum duration (Ullrich et al. 2021).

Cold air masses are typically confined to lower levels and therefore have been commonly defined using 700-hPa temperature (Grotjahn and Zhang 2017), 850-hPa temperature (Konrad and Colucci 1989; Colucci et al. 1999), or surface air temperature (Walsh et al. 2001; Portis et al. 2006; Vavrus et al. 2006; Turner and Gyakum 2011; Westby et al. 2013; Ayarzagüena and Screen 2016; Smith and Sheridan 2020; Millin et al. 2022). Here, we have chosen to identify CAOs using 2-m temperature ($T_{2m}$) as it is terrain following and does not require an interpolation below ground level in regions with high terrain. This is important when considering the entirety of the continent. Furthermore, $T_{2m}$ is widely available as output from global climate models, which is key for enabling future research on projected changes in CAOs.

Prior to air mass identification, the daily averaged $T_{2m}$ values were first detrended to remove the linear component of the anthropogenic warming signal (Westby et al. 2013). Next, climatological means and standard deviations in $T_{2m}$ were computed for each day of the year at each grid cell. After testing multiple values, a 21-day running mean was applied to both the climatological means and standard deviations, as done in Grumm and Hart (2001). This was necessary to smooth out the impact of internal variability on the climatology prior to event identification. We then computed standardized $T_{2m}$ anomalies by subtracting this daily average $T_{2m}$ for a given day of the year and dividing by this standard deviation in $T_{2m}$ for a given day of the year at each grid cell. Calculating anomalies relative to this daily climatology rather than seasonal or monthly means is important for detecting events throughout the entire winter season (Gu et al. 2008; Grotjahn et al. 2016). These preprocessing steps of detrending and tracking on standardized anomalies were chosen as the perception of cold, as well as its impacts on society, agriculture, and infrastructure, is highly dependent on geographic location, intraseasonal variability, and the baseline climate. Furthermore, for future identification of CAOs in other datasets or climate

TABLE 1. Various combinations of the input values (right column) for the parameters of threshold, minimum size, minimum overlap, and radius (left column) that were tested to identify and track cold air masses using TEs.

| Parameter | Tested input values |
|---|---|
| Threshold | $-1.5\sigma$, $-1.75\sigma$, $-2\sigma$ |
| Min size | 800–3000 grid cells (100 or 200 gridcell intervals) |
| Min overlap | 20%–80% (10% intervals) |
| Radius | 0°, 1°, 2°, 3° |

model simulations, this metric enables a universal definition regardless of mean model bias or future climate change.

The required inputs for the DetectBlobs and StitchBlobs kernels of TE were the threshold of the $T_{2m}$ standardized anomalies, the minimum number of grid cells for a contiguous feature to be flagged, the minimum duration of an event, the minimum spatial overlap between time steps to be identified as a single feature, and the radius of influence in great circle degrees per grid cell. The radius of influence refers to how far the impact of a flagged grid cell extends in all directions. For example, with a radius of 1° per grid cell, every grid cell within 1 great circle degree of a flagged grid cell (where the standardized anomaly is less than $-2\sigma$) would also be flagged. This effectively filled in gaps and smoothed the boundaries of the detected region. A 3-day minimum duration was used for all combinations, as most studies define a 2–5-day minimum duration criteria for CAOs (Walsh et al. 2001; Westby et al. 2013; Ayarzagüena and Screen 2016; Papritz and Spengler 2017; Smith and Sheridan 2020; Millin et al. 2022). Also, for the air mass tracking in this study, the data were subset to 25°–90°N to ensure that cold near-surface temperature anomalies in the subtropics associated with La Niña events would not be captured by the feature tracking algorithm. We tested a variety of combinations of the remaining input parameters as summarized in Table 1. For each combination, we evaluated the output trajectories, size, and time scale of detected air masses. A threshold of $-2\sigma$ was consistent with the definition of CAOs in many other studies, which used thresholds including $-2\sigma$, $-1.5\sigma$, or below the 10th percentile (Walsh et al. 2001; Portis et al. 2006; Westby et al. 2013; Ayarzagüena and Screen 2016; Screen et al. 2015; Smith and Sheridan 2020; Millin et al. 2022). We chose final input values based on comparisons of detected cold air masses' dates, trajectories, and intensities to documented CAO events. The inputs implemented in the final feature identification were $-2\sigma$, 1500 grid cells minimum size, 3-day minimum duration, radius of 1° per grid cell, and 50% overlap per daily time slice.

The final output of the feature tracking algorithm was a netCDF file containing the three-dimensional (longitude, latitude, time) domain of cold air masses from 1979 to 2020, with grid cell values corresponding to the unique identification (ID) for each individual air mass (see data availability statement for public access to this dataset). Each event additionally had an associated genesis date (first day of detection), lysis date (last day of detection), and duration. Next, we limited our analysis to continental air masses over North America. While cold air masses can form and propagate entirely over the ocean (Papritz and Spengler 2017), the aim of this study was to understand the processes important for the formation and movement of CAOs over land, where their societal impacts are most devastating. Thus, we required at least 50% of a detected air mass' lifespan be over land. This step removed cold air masses that were primarily marine, but moved briefly over land or followed a coastline. After postprocessing, there were a total of 410 North American cold air masses detected within the 1979–2020 period.

### c. *Thermodynamic energy budget*

A thermodynamic energy budget analysis within a nonfixed domain was conducted for all identified CAOs. The goal of this analysis is to gain an understanding of the role of synoptic-scale forcing in generating CAOs. The budget was computed at 850 hPa where surface cold air masses are still detectable (Turner and Gyakum 2011), in order to compute the budget on a fixed pressure level. It is also important to note that the results are sensitive to the pressure level chosen. To determine the sensitivity of the thermodynamic budget to the pressure level it was calculated on, it was also performed by calculating the terms at 925 hPa (not shown). Perhaps unsurprisingly, the residual term (including diabatic processes) played a larger role due to the closer proximity of the level to the surface and boundary layer. However, in regions of higher terrain (such as the Rocky Mountains), the 925-hPa surface is more extensively at or below the surface compared to 850 hPa, meaning the analysis would be performed using a larger amount of interpolated below-ground data that may not be representative of the atmosphere. Although there is no perfect level upon which to conduct the analysis, 850 hPa was ultimately chosen as a balance between minimizing issues with topography, while still adequately sampling the air masses, and is consistent with many previous studies (Konrad and Colucci 1989; Colucci et al. 1999). The energy budget was computed as follows, with overbars denoting the area average of each term over the airmass domain each day:

$$\overline{\frac{\partial T}{\partial t}} = \overline{-\mathbf{V}\cdot\nabla T} + \overline{\omega\sigma\frac{P}{R}} + \overline{\frac{1}{c_p}\frac{\partial H}{\partial t}}, \tag{1}$$

where $T$ is the temperature (K), $t$ is the time (s), $\mathbf{V}$ is the horizontal wind (m s$^{-1}$), $\nabla$ is the gradient operator, $\omega$ is the pressure velocity (Pa s$^{-1}$), $P$ is the constant pressure level (850 hPa), $R$ is the ideal gas constant for dry air (J kg$^{-1}$ K$^{-1}$), $c_p$ is the isobaric specific heat capacity (J kg$^{-1}$ K$^{-1}$), and $\partial H/\partial t$ is the diabatic heating rate (J kg$^{-1}$ s$^{-1}$). The static stability parameter $\sigma$ is defined as

$$\sigma = -\frac{1}{\rho}\frac{\partial \ln(\theta)}{\partial P}, \tag{2}$$

where $\rho$ is the density (kg m$^{-3}$), $\theta$ is the potential temperature (K), and the derivative is approximated as the difference between the 875- and 825-hPa surfaces. Density was calculated using the ideal gas law and thus expressed in terms of hourly 850-hPa temperature ($T$), constant 850-hPa pressure ($P$), and the ideal gas constant for dry air ($R$).

The term on the left-hand side of Eq. (1) is the temperature tendency (K day$^{-1}$), computed as the difference in instantaneous 850-hPa temperature at 0000 UTC between two consecutive days. Terms on the right-hand side are (from left to right) horizontal advection (K day$^{-1}$), the adiabatic term (K day$^{-1}$), and the diabatic term (K day$^{-1}$). The horizontal advection and adiabatic terms were computed from the hourly data between the 0000 UTC time steps and then daily averaged. The fourth term was computed as a residual, as in Colucci et al. (1999), Portis et al. (2006), and Turner and Gyakum (2011). Thus, it is important to note that in our calculation, this fourth term not only includes diabatic effects but also any discrepancies or errors. These discrepancies can result from the analysis increment (correction between the analysis and background forecast), interpolation from model levels to pressure levels, errors from representing the vertical derivative as a finite difference between 875 and 825 hPa in the calculation of $\sigma$, etc. This term will be interpreted to be primarily diabatic, though the data are not available to confirm the discrepancies are indeed small compared to the diabatic processes.

Spatial averages within the airmass boundary [overbars in Eq. (1)] are conducted over the CAO region identified on the subsequent day (shown schematically in Fig. 1). For example, if an air mass was detected on 1 December, the energy budget was computed on 30 November, but averaged within that airmass boundary on 1 December. This allowed us to capture the processes responsible for changes in shape, location, and size in the nonfixed CAO domain. This approach captures the entire area encompassing the airmass, such that there is not any assumption as to where the center is and where to apply a fixed box each day of the computation.

To understand which mechanisms were important for generating versus destroying cold air, we isolated the positive temperature tendency (warming) and negative temperature tendency (cooling) regions within the airmass boundaries as shown schematically in Fig. 1. The area-weighted averages for each of the terms on the right-hand side of Eq. (1) were computed separately each day within the warming and cooling regions of a given air mass. This prevented underestimation of processes in cases where one term contributed to both warming and cooling in separate regions of a CAO. The fractional area of the cold air mass that was warming versus cooling was also quantified by computing the ratio between the total area with positive versus negative temperature tendencies within the airmass boundary divided by the total airmass area for each day of its lifespan.

## 3. Results and discussion

### a. *Example CAO case: 18–23 January 1985*

From 18 to 23 January 1985, an intense CAO impacted the eastern United States, transiting from the Great Lakes to Florida. This CAO resulted in record-breaking minimum temperatures in the central and southeastern United States, had a rapid progression southward, and had devastating societal impacts (Colucci et al. 1999). We selected this case as an example to demonstrate the CAO tracking and thermodynamic energy budget calculations since Colucci et al. (1999) studied this event using a thermodynamic energy budget computed in a fixed domain. It was also one of many events documented in the literature that was used to assess the validity of the automated identification and thermodynamic energy budget methodology in our study.

At genesis, on 18 January, a CAO was identified over the Northwest Territories, parts of Nunavut and the Canadian Prairies, and extending into northern Ontario. In Fig. 2a, the CAO boundary is plotted with $T_{2m}$ anomalies, where the daily climatology is removed but the data are neither detrended nor standardized. This helps demonstrate that the air mass detected using standardized data was composed of genuinely cold air and that the entirety of the transiting cold air mass was encompassed by the detected boundary. In the midtroposphere, there were large positive 500-hPa geopotential height ($Z_{500}$) anomalies over Baffin Bay and the central Arctic consistent with a negative AO pattern (Fig. 2g). There was also anomalously high $Z_{500}$ observed over the west coast of North America and anomalously low $Z_{500}$ observed over northern Ontario extending south to the Gulf Coast (Fig. 2g). Anticyclonic circulation in sea level pressure (SLP) is observed downstream of the positive $Z_{500}$ anomaly (Fig. 2d). There was also a weak cyclone observed offshore of Labrador and east of the overlying trough in $Z_{500}$ (Fig. 2d). This circulation pattern implies geostrophic cold air advection in the southern portion of the CAO boundary (Fig. 2d), which is confirmed by the computed horizontal temperature advections (Fig. 3d). The main source of cooling throughout the entire

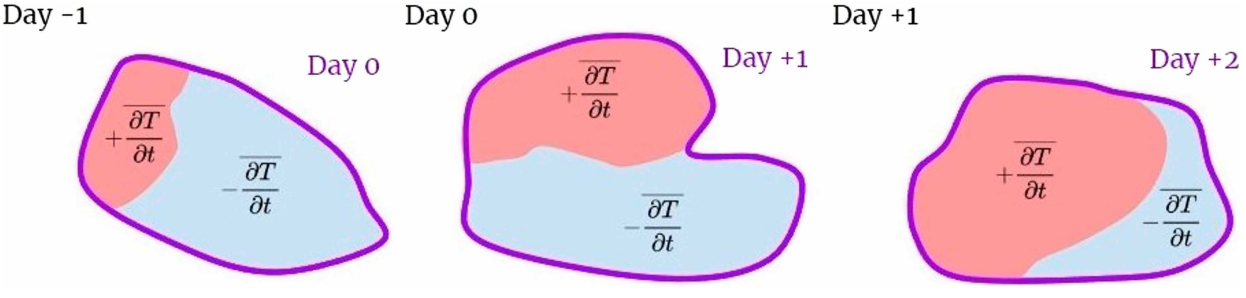


FIG. 1. Schematic illustrating how the feature-following thermodynamic energy budget was computed within an airmass boundary (purple contour) each day, as well as separation into positive (warming) and negative (cooling) temperature tendency regions. The thermodynamic energy budget on day −1 was analyzed over the day 0 airmass boundary.

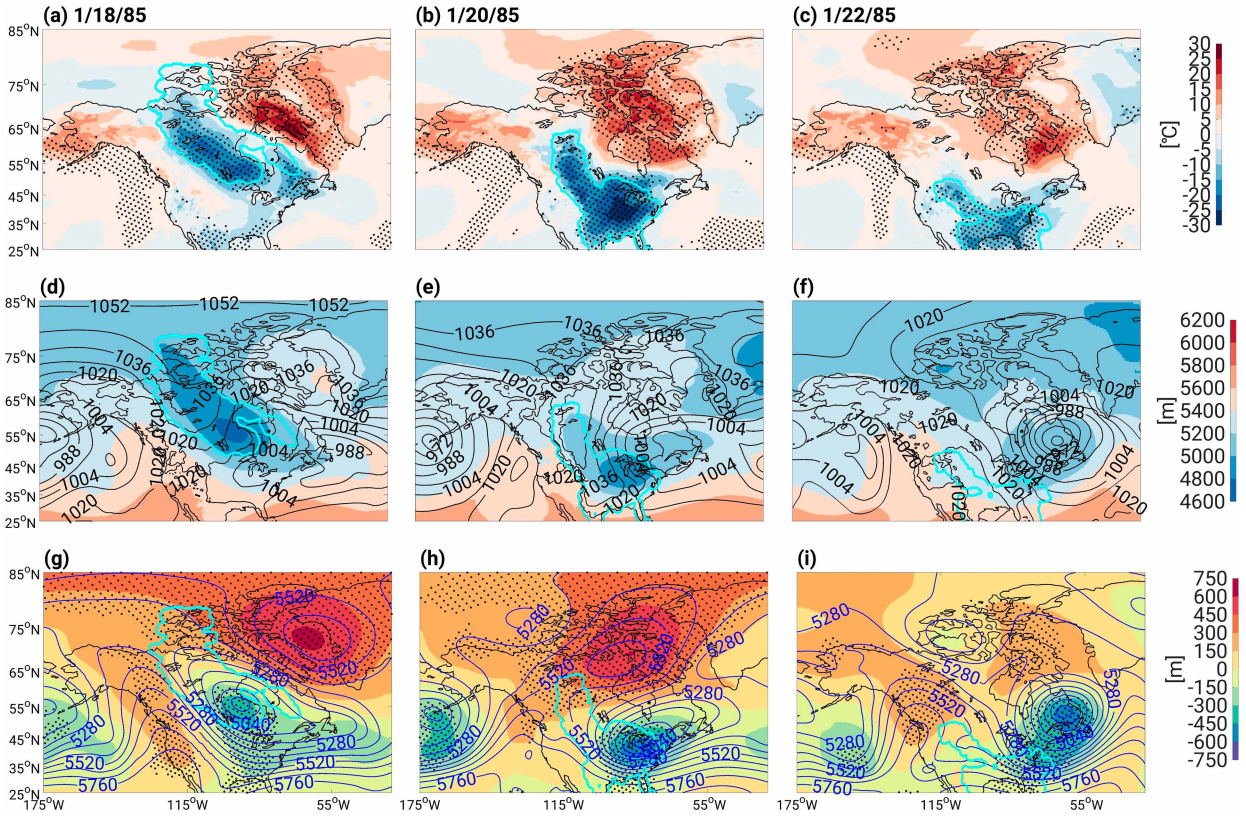


FIG. 2. (top) (from left to right) Daily average 2-m temperature anomalies (°C) on the 18, 20, and 22 Jan 1985. (middle) Black contours of daily average SLP at 8-hPa intervals, with colored contours of daily average 1000–500-hPa thickness (m) for those same 3 days. (bottom) Daily average 500-hPa height anomalies (m) in color and blue contours of 500-hPa heights at 80-m intervals. Cyan contours indicate the detected air mass on the same day. Stippling indicates significant anomalies at the 95% level (bootstrap resampling test).

life cycle was cold air advection. At genesis, 71% of the CAO was cooling, with an average rate of −6.7 K day$^{-1}$ over the cooling region (Fig. 4). This is contributed by both cold air advection (−2.3 K day$^{-1}$) and the residual term (−4.2 K day$^{-1}$) at genesis (Fig. 4). In the smaller warming region, the adiabatic term is the most positive at 6.6 K day$^{-1}$ and this is counteracted by residual (likely diabatic) cooling at −5.5 K day$^{-1}$ in this warming region (Fig. 4).

On 20 January 1985, the CAO expanded to encompass nearly the entire central and eastern United States, with a large region of $T_{2m}$ anomalies exceeding −20°C (Fig. 2b). The anticyclone traveled southward and intensified along the eastern edge of the Rockies (Fig. 2e), while the cyclone weakened, leading to strong geostrophic cold air advection in the Midwest and southeast United States (Fig. 2e). This was quantified in the temperature advection field, where strong cold air advection was found to coincide with the region of large negative temperature tendency (Figs. 3b,e). Averaged over the cooling region, temperature advection remained the dominant process, contributing −12.1 K day$^{-1}$ (Fig. 4). Within the warming region, the adiabatic term continued to be the most positive at 5.7 K day$^{-1}$ (Fig. 4). On this day, the residual term (2.6 K day$^{-1}$) in the cooling region was nearly equal in magnitude to the adiabatic term (2.2 K day$^{-1}$), and both acted in opposition to the strong cold air advection (Fig. 4).

On the second to last day of detection (22 January), the magnitude of the $T_{2m}$ anomalies decreased throughout the CAO (Fig. 2c). The cyclone in eastern Canada reintensified, but moved northward, away from the weakening anticyclone (Fig. 2f). Additionally, the warming region expanded to 45% of the total area on the second to last day of detection and 71% at lysis (Fig. 4). Significant negative temperature tendencies within the CAO domain were relegated to Florida and the Atlantic Ocean (Fig. 3c). Cold air advection peaked at −15.5 K day$^{-1}$ in the cooling region (Fig. 4). The strongest region of significant positive temperature tendencies was largely captured by the CAO boundary, whereas it was situated to the northeast of the event on prior days (Fig. 3c). The adiabatic term peaked at 11.1 K day$^{-1}$ in the warming region (Fig. 4). The residual term was slightly negative in the warming region and switched from positive to negative in the cooling region as the CAO approached lysis (Fig. 4). Finally, at lysis (23 January), the CAO diminished in both geographic extent and intensity.

### b. *Generalization of CAO events*

CAO events were sorted into three broad lysis regions based on the air mass' location on the last day of detection. Lysis locations on the last day of detection were determined for each air mass by calculating the percent area 1) north of

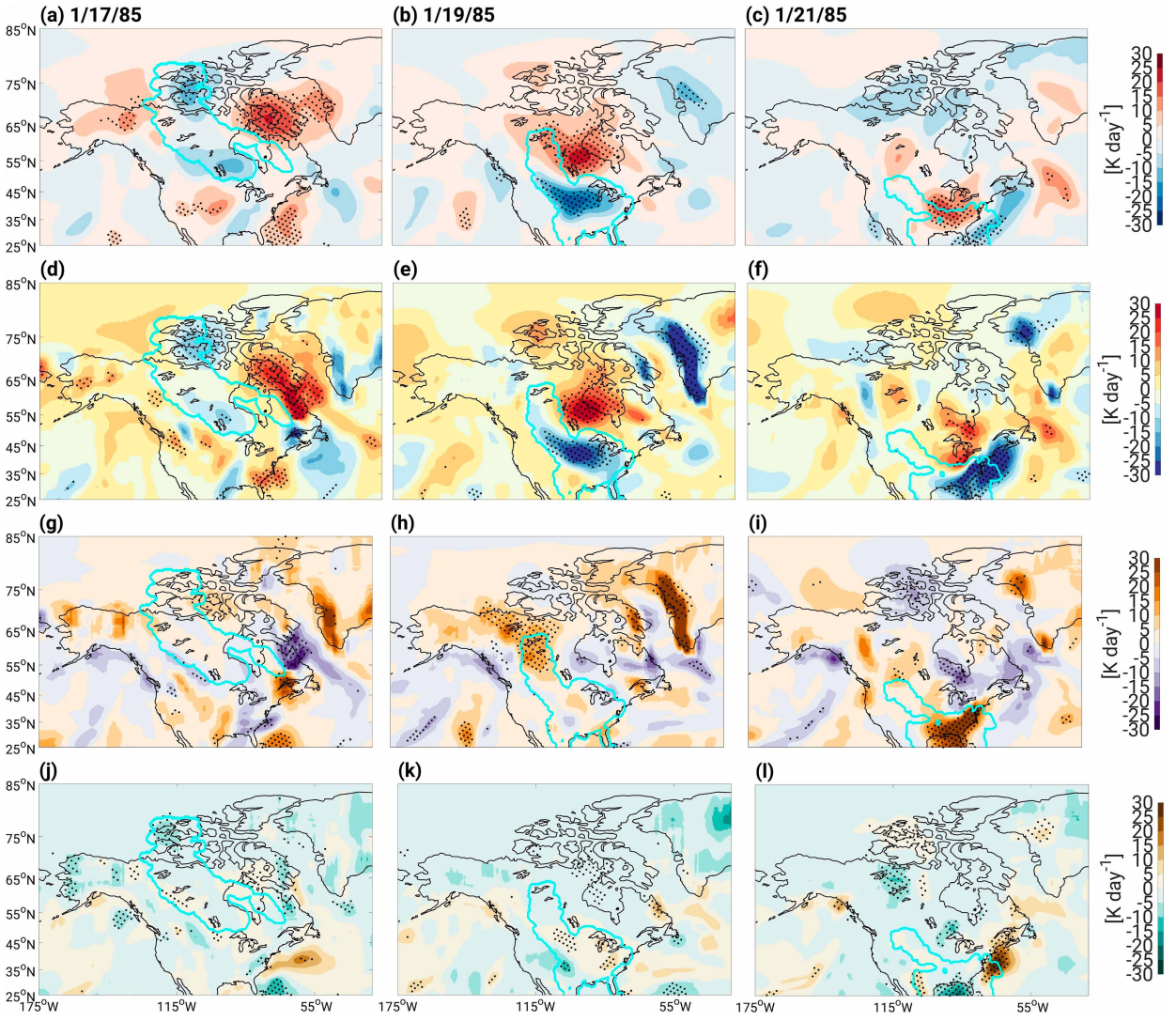


FIG. 3. As in Fig. 2, but columns are 17, 19, and 21 Jan, 1 day prior ($N - 1$) to the detected air mass (cyan contour). (from top to bottom) Temperature tendency (K day$^{-1}$), horizontal advection (K day$^{-1}$), adiabatic processes term (K day$^{-1}$), and residual, including diabatic processes, term (K day$^{-1}$) at the 850-hPa level. All displayed fields have been smoothed for visualization.

60°N (high latitude), 2) south of 60°N and west of 100°W (midlatitude west), or 3) south of 60°N and east of 100°W (midlatitude east) and shown schematically in Fig. 5. The longitude of 100°W was chosen as it is representative of the eastern boundary of the Rocky Mountains, which naturally bisects the continent and has a large influence on the development and transit of cold air masses (Colle and Mass 1995; Turner and Gyakum 2011). In total, 32% had the greatest percent area in the high latitudes (H), 40% in the midlatitudes west (W), and 28% in the midlatitudes east (E).

The processes governing CAO development and behavior across a large number of cases were assessed using the thermodynamic budgets computed for each identified CAO. As conducted for the January 1985 case study, the area-weighted average of each term in the thermodynamic budget equation [Eq. (1)] was computed over the negative temperature tendency region every day. To further generalize, these terms were averaged over the entire lifespan to get a value for the advection, adiabatic, and residual term for each air mass. The most negative of these terms was referred to as the dominant mechanism of cooling. The opposite was done to identify the dominant mechanism of warming over the positive temperature tendency region. In total, there are nine possible combinations of the dominant mechanism of cooling and warming. Over all CAO events (Table 2), horizontal advection (V) was the dominant cooling mechanism for 80.5% of air masses (330 events) and the dominant warming mechanism for 6.8% of detected air masses (28 events). Only 2.2% (9 events) had the adiabatic term (A) as the dominant cooling mechanism, but adiabatic warming was the leading warming mechanism for 90.5% of events (371 events). In 17.3% of events (71 events), the residual, including diabatic processes, term (D) was the dominant mechanism of cooling, and in

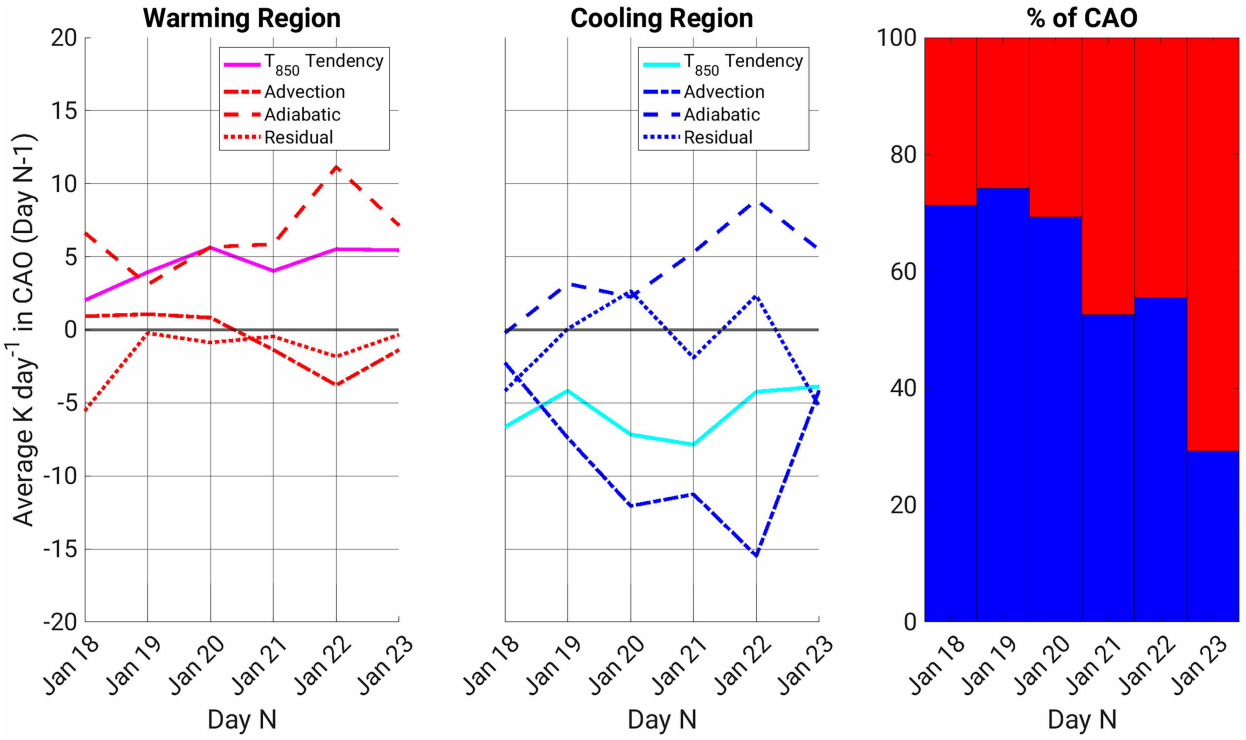


FIG. 4. Area-weighted average prior day ($N - 1$) temperature tendency (K day$^{-1}$; solid magenta, cyan lines), horizontal advection (K day$^{-1}$; dash–dotted red, blue lines), adiabatic processes term (K day$^{-1}$; dashed red, blue lines), and residual, including diabatic processes, term (K day$^{-1}$; dotted red, blue lines) within the airmass boundary at day $N$. The daily averages within the (left) warming region and (middle) cooling region. (right) The percentage of the air mass that was warming (red) or cooling (blue) each day.

2.7% of all events (11 events), it was the dominant mechanism of warming. Most of the events where residual (including diabatic) processes were dominant in cooling the air mass experienced lysis in the west or high latitudes.

The 410 detected air masses in the 1979–2021 period were then classified into 27 subcategories based on these lysis locations (H, E, or W), dominant mechanism of cooling (V, A, or D), and dominant mechanism of warming (V, A, or D), as summarized in Table 2. The following analysis was limited to events that would be classified as midlatitude CAOs (E or W) and subcategories that comprised at least 10 total detected air masses. This included three categories: eastern advective cooling and adiabatic warming (EVA), western advective cooling and adiabatic warming (WVA), and western diabatic cooling and adiabatic warming (WDA). These three subcategories comprised more than half of the total number of detected cold air masses and the vast majority of the midlatitude CAOs. The example CAO case from 18 to 23 January 1985 would be classified as an EVA event since it has lysis in the midlatitude east, cools primarily through advection, and warms primarily through adiabatic processes when considering the average over the entire duration.

Figure 6 shows the number of detected cold air masses each winter from 1979 to 2020. The mean for the 1979–2020 period was 9.76 cold air masses detected per winter. Winter 1985, 2009, and 2013 had the highest count at 16 individual cold

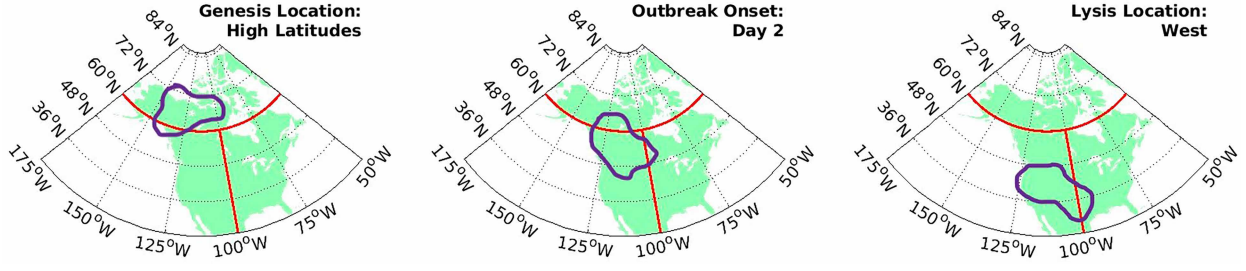


FIG. 5. Schematic illustrating how genesis location, onset date, and lysis location would be defined for a cold air mass (purple contour) based on the percentage of its area located in one of three broad regions: north of 60°N (high latitude), south of 60°N and west of 100°W (midlatitude west), and south of 60°N and east of 100°W (midlatitude east).

TABLE 2. Number of cold air masses detected in each subcategory, based on dominant mechanism of cooling, dominant mechanism of warming, and lysis location. The naming convention for each category was a three-letter abbreviation denoting the lysis location (H for high latitude, E for east, and W for west), and then a letter each for the dominant mechanism of cooling and warming (V for ad**v**ection, A for **a**diabatic processes, and D for **d**iabatic processes and resi**d**ual). Bold text and asterisks denote the three subcategories selected for further analysis.

| Dominant mechanism of cooling and warming | | Lysis in high lat (north of 60°N) | Lysis in midlat (east of 100°W) | Lysis in mid lat (west of 100°W) |
|---|---|---|---|---|
| Advection (V) | Advection (V) | 10 | 9 | 3 |
| Advection (V) | Adiabatic (A) | 87 | **100*** | **113*** |
| Advection (V) | Diabatic (D) | 1 | 2 | 5 |
| Adiabatic (A) | Advection (V) | 0 | 0 | 2 |
| Adiabatic (A) | Adiabatic (A) | 1 | 0 | 3 |
| Adiabatic (A) | Diabatic (D) | 0 | 2 | 1 |
| Diabatic (D) | Advection (V) | 3 | 0 | 1 |
| Diabatic (D) | Adiabatic (A) | 31 | 1 | **35*** |
| Diabatic (D) | Diabatic (D) | 0 | 0 | 0 |

air masses, and additionally, several winters had more than 12 individual cold air masses detected. The winters with the fewest cold air masses detected were 1997 with three and 2011 with two. In these low CAO winters, all events were WVA events.

Distributions of cold air mass duration in days are shown as solid colors in Fig. 7 for all detected cold air masses (All; Fig. 7a) and the subset of events falling into the three selected CAO subcategories (EVA, WVA, WDA; Figs. 7b–d). Durations were positively skewed for every subcategory. The mean durations of all three selected subcategories were 5.7, 6, and 5.6 days for EVA, WVA, and WDA, respectively. Permutation tests were implemented to determine if differences in mean duration for each subcategory were significant when compared to the mean duration of all detected cold air masses at an alpha value of 0.05. None of the subcategories significantly differed in mean duration from the All category at 5.4 days. For each event, we also defined a midlatitude CAO onset date as the first day more than half of the area of a cold air mass was situated south of 60°N (Fig. 5). This was done to distinguish antecedent conditions from what we consider to be midlatitude CAOs. An adjusted duration was then calculated as the number of days the air mass was detected starting at midlatitude onset rather than at CAO genesis. Consequently, high-latitude events have an adjusted duration of 0 days and are not considered CAOs by our criteria (Fig. 7a). Distributions of adjusted duration are displayed as outlines in Fig. 7. For All (Fig. 7a), the mean decreased from 5.4 to 3.9 days once adjusted duration was considered, which was significant at the 95% level (permutation test). However, differences in duration and adjusted duration did not meet the significance level for the three selected subcategories.

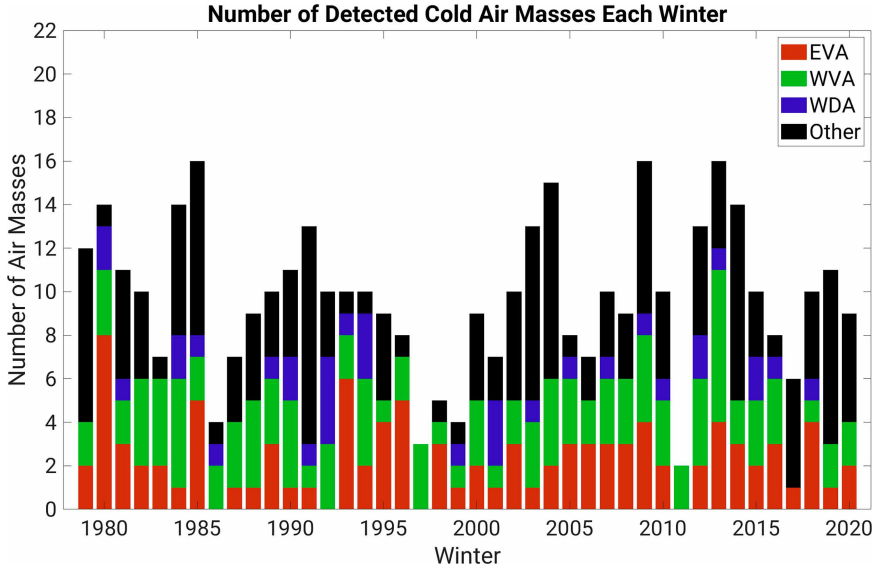


FIG. 6. The number of cold air masses detected each year separated into the number of EVA, WVA, or WDA events. All other categories (high-latitude air masses included) were grouped together as "Other."

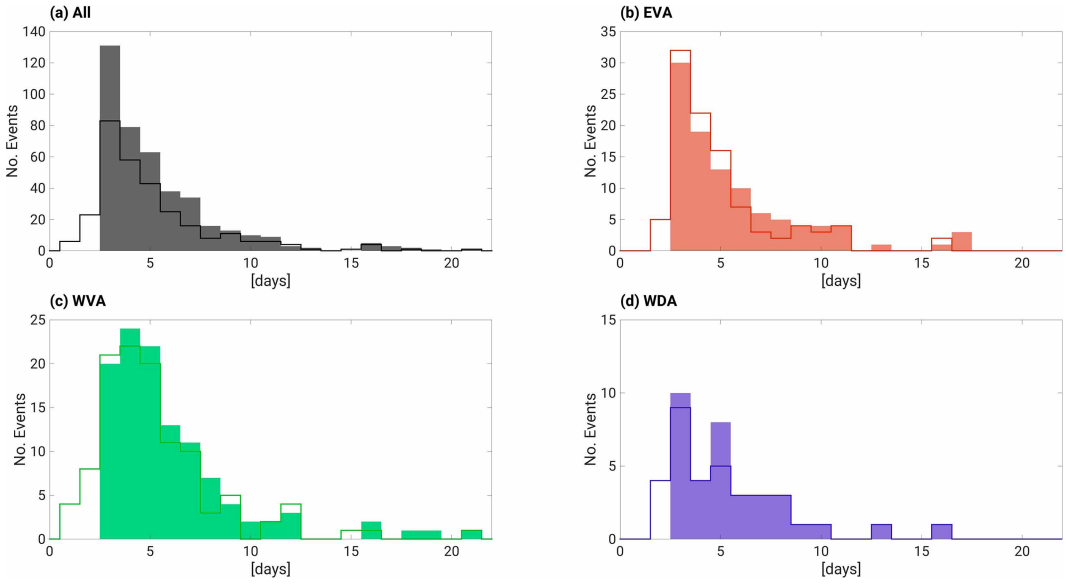


FIG. 7. Histograms of air mass duration (solid colors) and adjusted duration (outlines) in days for (a) all events, (b) EVA events, (c) WVA events, and (d) WDA events. Adjusted duration was calculated as the number of days the air mass was detected starting at midlatitude onset rather than genesis. High-latitude cases were excluded for adjusted duration in the (a) all histogram by definition.

Intensity was computed for each air mass as the area-weighted average climatological $T_{2m}$ anomaly (i.e., $T_{2m}$ with daily climatology removed, but not detrended or standardized) within the airmass boundary each day. These daily values were then averaged across all days to get a single intensity value per event. For the All category (Fig. 8a), the mean intensity was −6.9°C. EVA events were the most intense with a mean intensity of −8.6°C (Fig. 8b). The January 1985 CAO would be considered a relatively extreme EVA case at −12.5°C. WDA events (Fig. 8d) tended to be the least intense with a mean intensity of −5.1°C, and the mean intensity of WVA events was −6.8°C (Fig. 8c). For the All category and the three subcategories, the skewness of intensities generally resembled that of a Gaussian distribution. Permutation tests at the 95% level showed that the EVA and WDA subcategories differed in mean intensity when compared to the All category.

Peak intensities, represented as outlines in Fig. 8, were defined as the minimum $T_{2m}$ anomaly within the airmass boundary and over all days. This provided a measure of whether events experienced localized extreme temperatures compared to average-based intensities. The mean peak intensities for EVA, WVA, and WDA of −21.5°, −22.1°, and −18.1°C, respectively, significantly differed from −20.4°C for All. The WVA events were the most extreme category according to the mean peak intensity metric (Fig. 8c). This is in contrast to average-based intensities, from which EVA would be considered more extreme (Fig. 8b). The January 1985 CAO's peak intensity was −31.6°C making it one of the most intense CAOs overall by this metric (top 5%).

The number of days with a CAO detected at a given location is shown in Fig. 9 for each of the selected CAO subcategories. Black contours indicate the number of days that a CAO was detected at genesis for a given grid cell. The number of genesis days is the same as the number of events in a given category since each event only has one genesis day. The same was shown in color, except including all time steps over the entire lifespan of the CAOs. This provides a measure of the likelihood of the occurrence of a cold air mass of a given subcategory at a given location.

For EVA cases, the spatial footprint of these events extended throughout much of North America east of the Rockies at genesis and over the entire duration of events. The maximum in genesis is centered on the western edge of the Great Lakes while the maximum for the entire life cycle is displaced to the southeast (centered over the Great Lakes). This could indicate that many events experience a southeastward transit. However, with the large spread in locations, it is likely that there are a range of event trajectories included in this category. For example, in the January 1985 case described above, genesis occurred in the high latitudes before transit and expansion across the southeastern United States. This was consistent with the traditional mechanism of a cold-core anticyclone intensifying and moving southward, where it ultimately decays in response to subsidence warming (Dallavalle and Bosart 1975; Dunn 1987; Colle and Mass 1995; Colucci et al. 1999). The genesis region of these events to the lee of the Rockies suggests some WVA events could be subject to cold air damming as the CAOs surge from northwest Canada into the interior United States if certain conditions (i.e., accompanying cold-core anticyclone) are met (Dunn 1987; Colle and Mass 1995; Turner and Gyakum 2011).

At both genesis and over the full life cycle, WVA CAOs were generally concentrated over the Rocky Mountains and interior west, stretching from Alaska south to Mexico. The

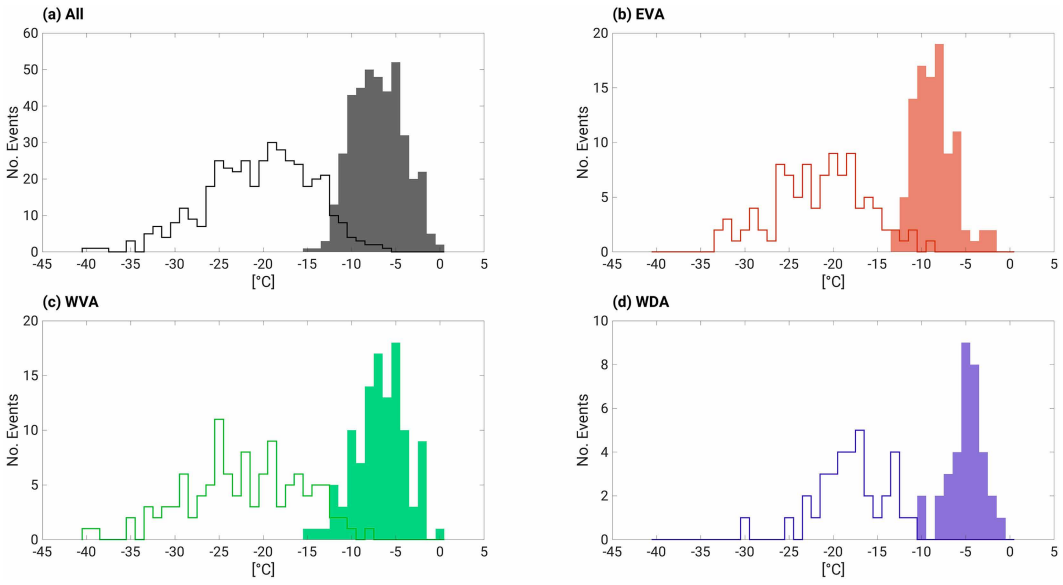


FIG. 8. As in Fig. 7, but for intensities (°C) in solid colors and peak intensities (°C) in outlines.

values for WVA events (Fig. 9b) were higher than other categories because more events fall into this category (Table 2). The highest values were centered over north-central California; however, these events span the entirety of the western United States and Canada. WDA events (Fig. 9c) were generally more geographically confined than WVA events. WDA CAOs (Fig. 9c) were concentrated in the interior west regions of the United States and did not shift much at all from their genesis region.

To understand the differing mechanisms responsible for initiating CAOs, we conducted composites of $Z_{500}$, SLP, $T_{850}$, and wind vectors at 850 hPa ($\mathbf{V}_{850}$) at outbreak onset into the midlatitudes for each CAO subcategory. Compositing was conducted at onset rather than at genesis in order to capture conditions associated with the dislodging of cold air masses from the Arctic that eventually transition into the midlatitudes; however, these results were qualitatively similar when genesis was composited.

For EVA events, there was significant anomalous 500-hPa ridging centered over the Beaufort Sea at onset, which extended to high latitudes over western North America and into the Arctic (Fig. 10a). The amplified ridge is accompanied by anomalous troughing over eastern North America, which is indicative of a positive PNA-like pattern that favors cold air outbreaks in the eastern United States (Leathers et al. 1991). Downstream of this anomalous ridging, a broad area of significant positive SLP anomalies was oriented northwest–southeast across the northern Rockies into the Midwest, resulting in an area of anticyclonic lower-tropospheric flow centered east of the Rockies (Fig. 10b). While it cannot be confirmed from this analysis alone, this may indicate cold air damming occurs for some EVA events that transit from northwest Canada into the central and eastern United States at onset. Located east of this area of higher SLP were significant negative $T_{850}$ anomalies, with northwesterly $\mathbf{V}_{850}$ advecting cold air to the east of the Rockies (Fig. 10c). This region of cold air advection was associated with an anomalous upper-level trough centered over the Great Lakes, with anomalies exceeding −80 m (Fig. 10a). There were also negative SLP anomalies over eastern Canada, which in conjunction with the anticyclonic circulation over the Midwest could act to funnel cold air southward across Hudson Bay into eastern North America. This funneling of cold air by an anticyclone–cyclone couplet as well as the placement of the upper-level ridge over the western North America are consistent with known mechanisms of CAOs impacting the eastern United States (e.g., Dallavalle and Bosart 1975; Konrad 1996; Colucci et al. 1999).

The WVA subcategory had anomalously high heights along and just upstream of the ridge axis in the eastern North Pacific, with a trough over the western United States (Fig. 10d). Positive SLP anomalies were located over much of the western United States and Canada (Fig. 10e). Both of these features were similar to the setup of CAOs in the California Central Valley described in Grotjahn and Zhang (2017), with a large-scale meteorological pattern in $Z_{500}$ resembling a negative PNA and positive SLP anomalies in the Gulf of Alaska. There were cold anomalies over the entire western United States, with the deepest $T_{850}$ anomalies located over British Columbia, Alberta, and most of Saskatchewan (Fig. 10f). Winds at 850 hPa indicate cold air advection over Alberta and Saskatchewan as well as around the anticyclone off the coast of Baja California. The locations of the low-level cold air advection, as well as the importance of subsidence and adiabatic warming, are also similar to those processes described in Grotjahn and Zhang (2017).

Finally, the WDA subcategory had ridging over the Pacific Northwest and significant troughing to the east of the CAO region (Fig. 10g). Between these $Z_{500}$ anomalies, there were positive SLP anomalies that coincide with the negative anomalies in $T_{850}$ (Fig. 10h). Unlike the other categories, winds at 850 hPa were largely zero over the CAO (Fig. 10i), consistent

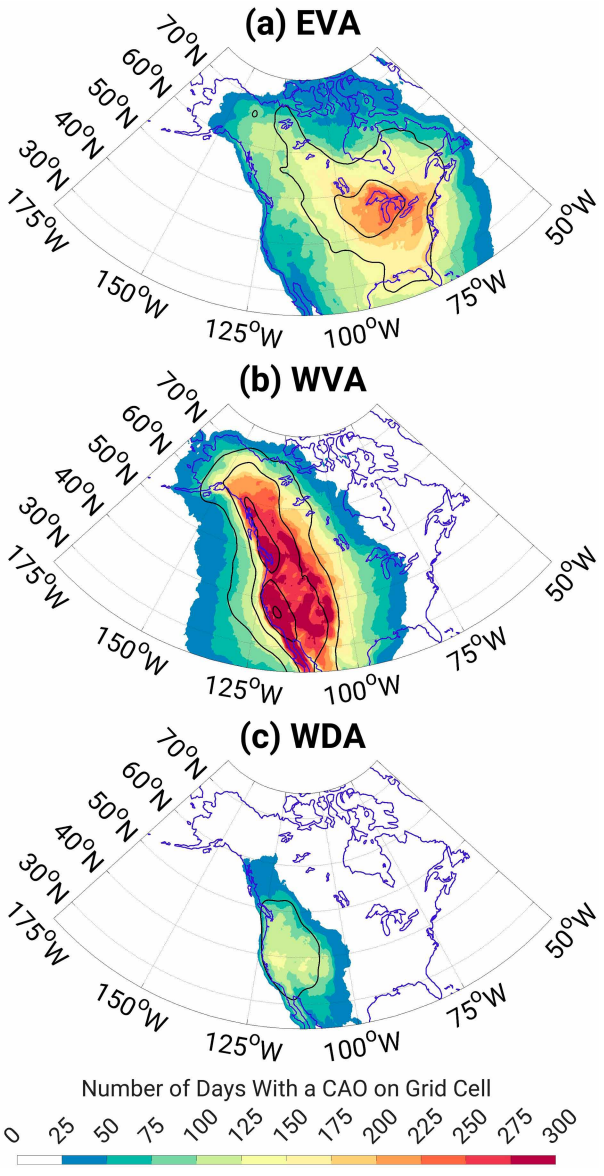


FIG. 9. Solid colors represent the number of days where a CAO was located at a given location for (a) EVA events, (b) WVA events, and (c) WDA events. Black contours indicate the same, but only taking into account the first day of detection (genesis) for each CAO in a given subcategory, with a contour interval of 10 days. Contours have been smoothed for visualization.

with advection not playing a driving role in these events. The dominant mechanism of cooling in these events was the residual term. Given that these events were associated with high pressure over the genesis region, enhanced radiative cooling in association with clear skies may play a role in generating these events. Furthermore, these events may be influenced by localized mesoscale processes such as valley cold pools even though they are synoptic scale in terms of their overall spatial extent (Reeves and Stensrud 2009).

Both the NAO and PNA have been associated with CAOs in North America (e.g., Walsh et al. 2001; Westby et al. 2013; Grotjahn et al. 2016). Table 3 shows the mean standardized daily NAO and PNA indices for each subcategory at four different points of the CAO life cycle, genesis, midlatitude onset, the midpoint between onset and lysis, and lysis. The mean NAO indices are insignificant across all three subcategories at the 95% level as determined by a two-sided $z$ test. For the PNA, there was a divide between the advective cooling eastern category EVA associated with positive PNA and advective cooling western subcategory WVA associated with negative PNA. For EVA, these standardized indices were significant throughout the entire life cycle, peaking at 2.13 at onset. The mean standardized indices at genesis, midpoint, and lysis were also much larger in magnitude compared to the two western subcategories. The mean standardized PNA indices for WVA were all negative and significant at all points except lysis. The mean standardized daily PNA index decreased for WVA throughout the life cycle, peaking at −0.64 at genesis, followed by −0.51 at onset, −0.48 at midpoint, and −0.28 at lysis. This suggests a more direct connection between the PNA and advection-driven CAOs compared to the NAO.

## 4. Conclusions

A feature tracking approach was used in this study to identify, track, and evaluate the mechanisms driving North American cold air outbreaks (CAOs) throughout their life cycle. The automated feature tracking algorithm TempestExtremes (TE) from Ullrich et al. (2021) allowed for detection of cold air masses based on standardized $T_{2m}$ anomalies. We used the CAO identified on 18–22 January 1985 as an example to demonstrate how the methodology captures our events.

CAOs were then generalized based on the dominant mechanisms of warming and cooling. This analysis was conducted using a unique approach where the thermodynamic energy budget was computed in a nonfixed feature tracked domain. Over each day of the CAO life cycle, grid points were defined as warming or cooling based on the sign of the temperature tendency in the prior day. To identify the important processes driving CAO changes, we quantified the temperature advection, adiabatic processes, and residual (including diabatic processes) within these warming and cooling regions. For CAOs with lysis in the midlatitudes, we found the majority of events fell into three main subcategories, namely, eastern advective cooling and adiabatic warming (EVA), western advective cooling and adiabatic warming (WVA), and western diabatic cooling and adiabatic warming (WDA). As noted by Turner et al. (2013), different processes can act at different levels within an air mass. In this study, we chose to conduct our thermodynamic analysis at 850 hPa; however, choosing a level nearer to the surface could result in different processes being more dominant for a given case. In regions of higher topography where the 850-hPa surface would be closer to the ground, we might expect diabatic cooling to play a stronger role. This could explain the existence of diabatic cooling and advective warming cases in western but not in eastern North America. The generalizations presented here should thus not be interpreted to mean that diabatic warming and cooling is less important overall for CAOs, but rather that at 850-hPa advective cooling and adiabatic warming tend to be

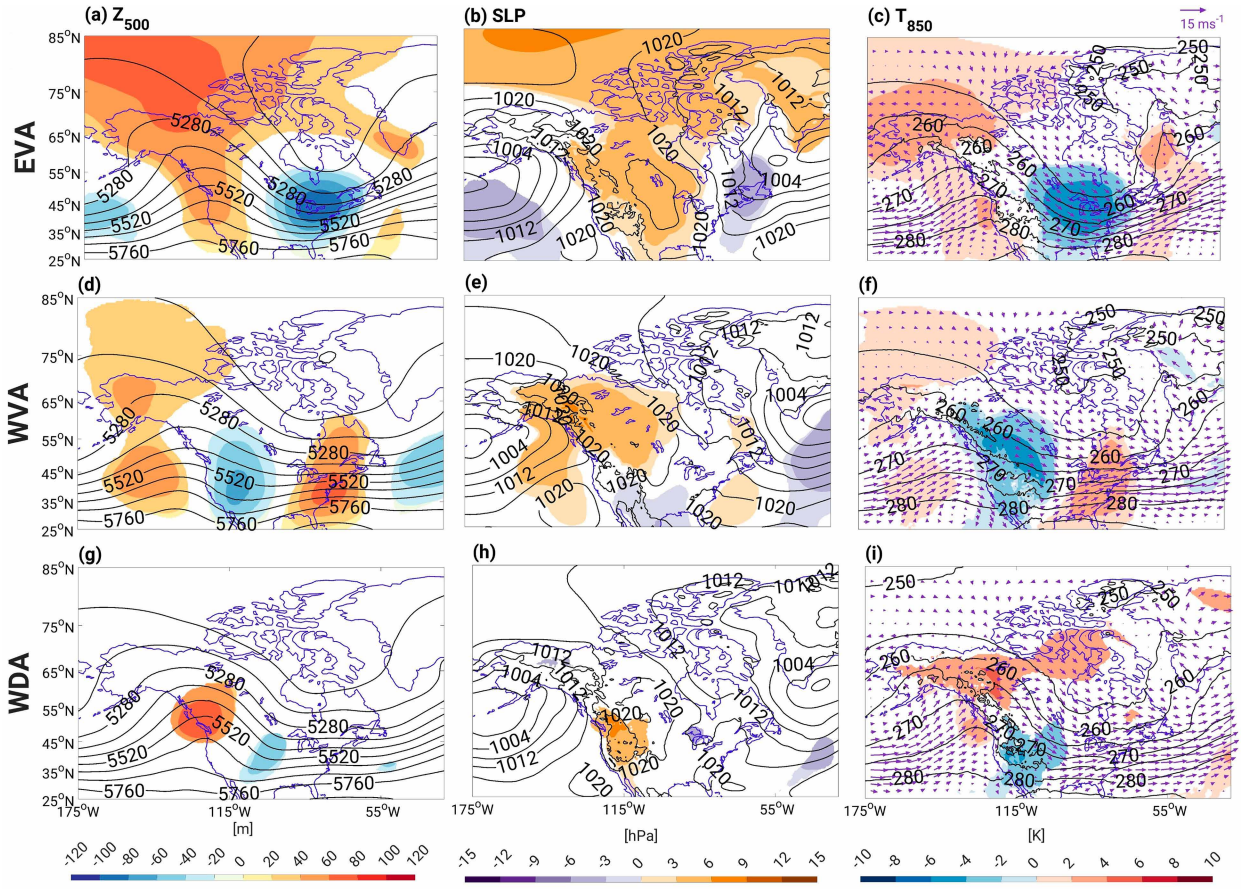


FIG. 10. Composites for three CAO subcategories: EVA, WVA, and WDA at outbreak onset. (left) 500-hPa geopotential height anomalies (m; color) and 500-hPa heights (m; black contours every 20 m). (middle) SLP anomalies (hPa; color) and SLP (hPa; black contours every 4 hPa). (right) $T_{850}$ anomalies (K; color), $T_{850}$ (K; black contours every 5 K), and $\mathbf{V}_{850}$ (m s$^{-1}$; purple vectors). Colored contours indicate significance in anomalies based on a bootstrap resampling methodology, at the 95% level, whereas white indicates insignificance.

the most important processes. On a case-by-case basis, this budget could be computed on a series of levels within the cold air mass to dig more deeply into the vertical structure of the mechanisms responsible.

The remainder of our analysis focused on the three CAO subcategories (i.e., EVA, WVA, and WDA). The average duration of all events was 5.4 days with no significant differences in duration between all events and the three subcategories. There were significant differences in average and peak intensities between subcategories. When considering average-based intensity, the EVA CAOs were the most extreme. When considering peak intensity, WVA CAOs were the most extreme. This may be indicative of the influence of topography for western events, as cold dense air may reach localized extreme cold in the deep valleys of the Rockies, which would be too small to skew the average-based intensities but would be captured when using minima (Reeves and Stensrud 2009). The number of cases detected at a given location also differed between subcategories. EVA CAOs have a broad footprint in location both at genesis and throughout their life cycle that encompasses the majority of North America east of the Rockies with a peak near the Great Lakes. WVA CAOs were widespread across the western continental United States and Canada. WDA CAOs were largely midlatitude features, with little high latitude presence. Due to the localized impact and lower intensity of these WDA events, an open question remains whether these constitute CAOs. If WDA events are found to be influenced primarily by mesoscale diabatic processes in the mountains, this could serve as an argument against considering these CAOs in future work.

Composites of sea level pressure and geopotential height anomalies at onset, as well as evaluation of standardized NAO and PNA indices, provide additional insight into the mechanisms responsible for the differences between CAO subcategories. For EVA events, composites at onset showed significant upper-level ridging centered over Alaska, which resulted in a strong surface high over central North America, subsequent cold air advection, and a surface anticyclone–cyclone pair west of the Great Lakes leading to additional cold air advection into the eastern United States across and to the east of Hudson Bay. There was a positive PNA-like pattern at onset that continued throughout the life cycle of these events.

TABLE 3. A. Mean standardized daily NAO indices at genesis, midlatitude onset, midpoint between onset and lysis, and lysis for three CAO subcategories: EVA, WVA, and WDA. B. Mean standardized daily PNA teleconnection pattern indices at the same four points of the CAO life cycle, for the same three subcategories. Significance at the 95% level is represented by bold text and was determined by two-sided $z$ tests.

| | EVA | WVA | WDA |
|---|---|---|---|
| A. NAO | | | |
| Genesis | 0.05 | 0.12 | −0.01 |
| Onset | −0.06 | 0.05 | −0.02 |
| Midpoint | −0.02 | 0.23 | 0.04 |
| Lysis | 0.05 | 0.29 | 0.05 |
| B. PNA | | | |
| Genesis | **1.85** | **−0.64** | 0.13 |
| Onset | **2.13** | **−0.51** | 0.15 |
| Midpoint | **1.96** | **−0.48** | 0.15 |
| Lysis | **1.94** | −0.28 | 0.19 |

These CAOs were particularly intense as a result of these mechanisms. WVA events were associated with a negative PNA, strong upper-level high over the eastern North Pacific and Alaska, an upper-level low coinciding with the CAO, and positive SLP anomalies over much of Alaska and western Canada at onset facilitating advection of cold air from Alberta and Saskatchewan. As in the EVA cases, lysis occurred due to adiabatic effects. WVA cases were additionally associated with the strongest peak intensities. This may be in part due to WVA events moving into regions that are on-average warmer compared to the locations of EVA events, allowing for the minimum temperature anomalies to reach more extreme values. Unlike EVA, WVA events also do not advect over any large bodies of water such as the Great Lakes or Hudson Bay. Finally, WDA events were associated with high surface pressure in the genesis region, weak circulation anomalies allowing for maintenance of the CAO once diabatic cooling is initiated, and lower intensities than other CAOs induced by cold air advection.

In this study, we have focused on historical CAO events. These events were identified based on standardized anomalies in 2-m temperatures. This field is widely available as output from both reanalysis and global climate model simulations. Application of this methodology to global climate model simulations over the historical period can enable a process-oriented evaluation to determine how well CAOs are simulated as compared to ERA5. Furthermore, applying this methodology to single-model initial-condition large ensembles can enable a robust analysis of trends in CAOs over the historical period, taking into account internal variability. Finally, the impact of anthropogenic forcing on CAOs can be assessed by applying this method to CMIP6 simulations with projected anthropogenic forcing.

*Acknowledgments.* The authors are grateful for the valuable feedback and suggestions from the three anonymous reviewers, which have improved the final manuscript. Computations for this research were conducted using supercomputing resources provided by the National Center for Atmospheric Research (NCAR) Casper Computing Cluster and resources from The Pennsylvania State University Institute for Computational and Data Sciences (ICDS). This content is solely the responsibility of the authors and does not necessarily represent the views of the ICDS. This research was supported by NSF Grants AGS-2236771 and AGS-2148567.

*Data availability statement.* ERA5 data are made available by the ECMWF through the Copernicus data storage system at https://doi.org/10.24381/cds.adbb2d47 and https://doi.org/10.24381/cds.bd0915c6. TempestExtremesV2.1 (Ullrich et al. 2021) is available at climate.ucdavis.edu/tempestextremes.php. Cold air masses identified over the entire Northern Hemisphere created for this study, as well as each term in the thermodynamic energy budget, are openly available from the Penn State DataCommons at https://doi.org/10.26208/S9XA-NY60.

## REFERENCES

Ackerman, S. A., A. S. Bachmeier, K. Strabala, and M. Gunshor, 2005: A unique satellite perspective of the 13–14 January 2004 record cold outbreak in the northeast. *Wea. Forecasting*, **20**, 222–225, https://doi.org/10.1175/WAF842.1.

Ayarzagüena, B., and J. A. Screen, 2016: Future Arctic sea ice loss reduces severity of cold air outbreaks in midlatitudes. *Geophys. Res. Lett.*, **43**, 2801–2809, https://doi.org/10.1002/2016GL068092.

Bailey, C. M., G. Hartfield, G. M. Lackmann, K. Keeter, and S. Sharp, 2003: An objective climatology, classification scheme, and assessment of sensible weather impacts for Appalachian cold-air damming. *Wea. Forecasting*, **18**, 641–661, https://doi.org/10.1175/1520-0434(2003)018<0641:AOCCSA>2.0.CO;2.

Balaguru, K., and Coauthors, 2020: Characterizing tropical cyclones in the Energy Exascale Earth System Model version 1. *J. Adv. Model. Earth Syst.*, **12**, e2019MS002024, https://doi.org/10.1029/2019MS002024.

Barnston, A. G., and R. E. Livezey, 1987: Classification, seasonality, and persistence of low-frequency atmospheric circulation patterns. *Mon. Wea. Rev.*, **115**, 1083–1126, https://doi.org/10.1175/1520-0493(1987)115%3C1083:CSAPOL%3E2.0.CO;2.

Bell, G. D., and L. F. Bosart, 1988: Appalachian cold-air damming. *Mon. Wea. Rev.*, **116**, 137–161, https://doi.org/10.1175/1520-0493(1988)116%3C0137:ACAD%3E2.0.CO;2.

Biernat, K. A., L. F. Bosart, and D. Keyser, 2021: A climatological analysis of the linkages between tropopause polar vortices, cold pools, and cold air outbreaks over the central and eastern United States. *Mon. Wea. Rev.*, **149**, 189–206, https://doi.org/10.1175/MWR-D-20-0191.1.

Bolinger, R. A., and Coauthors, 2022: An assessment of the extremes and impacts of the February 2021 south-central U.S. Arctic outbreak, and how climate services can help. *Wea. Climate Extremes*, **36**, 100461, https://doi.org/10.1016/j.wace.2022.100461.

Cellitti, M. P., J. E. Walsh, R. M. Rauber, and D. H. Portis, 2006: Extreme cold air outbreaks over the United States, the polar vortex, and the large-scale circulation. *J. Geophys. Res.*, **111**, D02114, https://doi.org/10.1029/2005JD006273.

Chavas, D. R., K. A. Reed, and J. A. Knaff, 2017: Physical understanding of the tropical cyclone wind-pressure relationship.

*Nat. Commun.*, **8**, 1360, https://doi.org/10.1038/s41467-017-01546-9.

Colle, B. A., and C. F. Mass, 1995: The structure and evolution of cold surges east of the Rocky Mountains. *Mon. Wea. Rev.*, **123**, 2577–2610, https://doi.org/10.1175/1520-0493(1995)123%3C2577:TSAEOC%3E2.0.CO;2.

Colucci, S. J., D. P. Baumhefner, and C. E. Konrad II, 1999: Numerical prediction of a cold-air outbreak: A case study with ensemble forecasts. *Mon. Wea. Rev.*, **127**, 1538–1550, https://doi.org/10.1175/1520-0493(1999)127%3C1538:NPOACA%3E2.0.CO;2.

Curry, J., 1983: On the formation of continental polar air. *J. Atmos. Sci.*, **40**, 2278–2292, https://doi.org/10.1175/1520-0469(1983)040%3C2278:OTFOCP%3E2.0.CO;2.

Dallavalle, J. P., and F. L. Bosart, 1975: A synoptic investigation of anticyclogenesis accompanying North American polar air outbreaks. *Mon. Wea. Rev.*, **103**, 941–957, https://doi.org/10.1175/1520-0493(1975)103%3C0941:ASIOAA%3E2.0.CO;2.

Dunn, L., 1987: Cold air damming by the front range of the Colorado Rockies and its relationship to locally heavy snows. *Wea. Forecasting*, **2**, 177–189, https://doi.org/10.1175/1520-0434(1987)002%3C0177:CADBTF%3E2.0.CO;2.

Grotjahn, R., and R. Zhang, 2017: Synoptic analysis of cold air outbreaks over the California Central Valley. *J. Climate*, **30**, 9417–9433, https://doi.org/10.1175/JCLI-D-17-0167.1.

——, and Coauthors, 2016: North American extreme temperature events and related large scale meteorological patterns: A review of statistical methods, dynamics, modeling, and trends. *Climate Dyn.*, **46**, 1151–1184, https://doi.org/10.1007/s00382-015-2638-6.

Grumm, R. H., and R. Hart, 2001: Standardized anomalies applied to significant cold season weather events: Preliminary findings. *Wea. Forecasting*, **16**, 736–754, https://doi.org/10.1175/1520-0434(2001)016<0736:SAATSC>2.0.CO;2.

Gu, L., P. J. Hanson, W. M. Post, D. P. Kaiser, B. Yang, R. Nemani, S. G. Pallardy, and T. Meyers, 2008: The 2007 eastern US spring freeze: Increased cold damage in a warming world? *BioScience*, **58**, 253–262, https://doi.org/10.1641/B580311.

Hartig, K., E. Tziperman, and C. P. Loughner, 2023: Processes contributing to North American cold air outbreaks based on air parcel trajectory analysis. *J. Climate*, **36**, 931–943, https://doi.org/10.1175/JCLI-D-22-0204.1.

Hersbach, H., and Coauthors, 2020: The ERA5 global reanalysis. *Quart. J. Roy. Meteor. Soc.*, **146**, 1999–2049, https://doi.org/10.1002/qj.3803.

Iwasaki, T., T. Shoji, Y. Kanno, M. Sawada, M. Ujiie, and K. Takaya, 2014: Isentropic analysis of polar cold airmass streams in the Northern Hemispheric winter. *J. Atmos. Sci.*, **71**, 2230–2243, https://doi.org/10.1175/JAS-D-13-058.1.

Konrad, C. I., II, 1996: Relationships between the intensity of cold-air outbreaks and the evolution of synoptic and planetary-scale features over North America. *Mon. Wea. Rev.*, **124**, 1067–1083, https://doi.org/10.1175/1520-0493(1996)124%3C1067:RBTIOC%3E2.0.CO;2.

Konrad, C. E., II, and S. J. Colucci, 1989: An examination of extreme cold air outbreaks over eastern North America. *Mon. Wea. Rev.*, **117**, 2687–2700, https://doi.org/10.1175/1520-0493(1989)117%3C2687:AEOEOECA%3E2.0.CO;2.

Leathers, D. J., B. Yarnal, and M. A. Palecki, 1991: The Pacific/North American teleconnection pattern and United States climate. Part I: Regional temperature and precipitation associations. *J. Climate*, **4**, 517–528, https://doi.org/10.1175/1520-0442(1991)004%3C0517:TPATPA%3E2.0.CO;2.

Matthias, V., and M. Kretschmer, 2020: The influence of stratospheric wave reflection on North American cold spells. *Mon. Wea. Rev.*, **148**, 1675–1690, https://doi.org/10.1175/MWR-D-19-0339.1.

McClenny, E. E., P. A. Ullrich, and R. Grotjahn, 2020: Sensitivity of atmospheric river vapor transport and precipitation to uniform sea surface temperature increases. *J. Geophys. Res. Atmos.*, **125**, e2020JD033421, https://doi.org/10.1029/2020JD033421.

Messori, G., and D. Faranda, 2023: On the systematic occurrence of compound cold spells in North America and wet or windy extremes in Europe. *Geophys. Res. Lett.*, **50**, e2022GL101008, https://doi.org/10.1029/2022GL101008.

——, R. Caballero, and M. Gaetani, 2016: On cold spells in North America and storminess in western Europe. *Geophys. Res. Lett.*, **43**, 6620–6628, https://doi.org/10.1002/2016GL069392.

Millin, O. T., J. C. Furtado, and J. B. Basara, 2022: Characteristics, evolution, and formation of cold air outbreaks in the Great Plains of the United States. *J. Climate*, **35**, 4585–4602, https://doi.org/10.1175/JCLI-D-21-0772.1.

Papritz, L., and T. Spengler, 2017: A Lagrangian climatology of wintertime cold air outbreaks in the Irminger and Nordic seas and their role in shaping air-sea heat fluxes. *J. Climate*, **30**, 2717–2737, https://doi.org/10.1175/JCLI-D-16-0605.1.

Patricola, C. M., J. P. O'Brien, M. D. Risser, A. M. Rhoades, T. A. O'Brien, P. A. Ullrich, D. A. Stone, and W. D. Collins, 2020: Maximizing ENSO as a source of western US hydroclimate predictability. *Climate Dyn.*, **54**, 351–372, https://doi.org/10.1007/s00382-019-05004-8.

Pinheiro, M. C., P. A. Ullrich, and R. Grotjahn, 2019: Atmospheric blocking and intercomparison of objective detection methods: Flow field characteristics. *Climate Dyn.*, **53**, 4189–4216, https://doi.org/10.1007/s00382-019-04782-5.

Portis, D. H., M. P. Cellitti, W. L. Chapman, and J. E. Walsh, 2006: Low-frequency variability and evolution of North American cold air outbreaks. *Mon. Wea. Rev.*, **134**, 579–597, https://doi.org/10.1175/MWR3083.1.

Rackley, J. A., and J. A. Knox, 2016: A climatology of southern Appalachian cold-air damming. *Wea. Forecasting*, **31**, 419–432, https://doi.org/10.1175/WAF-D-15-0049.1.

Reeves, H. D., and D. J. Stensrud, 2009: Synoptic-scale flow and valley cold pool evolution in the western United States. *Wea Forecasting*, **24**, 1625–1643, https://doi.org/10.1175/2009WAF2222234.1.

Roberts, M. J., and Coauthors, 2020: Impact of model resolution on tropical cyclone simulation using the HighResMIP–PRIMAVERA multimodel ensemble. *J. Climate*, **33**, 2557–2583, https://doi.org/10.1175/JCLI-D-19-0639.1.

Rogers, J. C., and R. V. Rohli, 1991: Florida citrus freezes and polar anticyclones in the Great Plains. *J. Climate*, **4**, 1103–1113, https://doi.org/10.1175/1520-0442(1991)004%3C1103:FCFAPA%3E2.0.CO;2.

Screen, J. A., C. Deser, and L. Sun, 2015: Reduced risk of North American cold extremes due to continued Arctic sea ice loss. *Bull. Amer. Meteor. Soc.*, **96**, 1489–1503, https://doi.org/10.1175/BAMS-D-14-00185.1.

Smith, E. T., and S. C. Sheridan, 2020: Where do cold air outbreaks occur, and how have they changed over time? *Geophys. Res. Lett.*, **47**, e2020GL086983, https://doi.org/10.1029/2020GL086983.

Tanaka, H. L., and M. F. Milkovich, 1990: A heat budget analysis of the polar troposphere in and around Alaska during the abnormal winter of 1988/89. *Mon. Wea. Rev.*, **118**,

1628–1639, https://doi.org/10.1175/1520-0493(1990)118%3C1628:AHBAOT%3E2.0.CO;2.

Turner, J. K., and J. R. Gyakum, 2011: The development of Arctic air masses in northwest Canada and their behavior in a warming climate. *J. Climate*, **24**, 4618–4633, https://doi.org/10.1175/2011JCLI3855.1.

——, J. Gyakum, and S. M. Milrad, 2013: A thermodynamic analysis of an intense North American arctic air mass. *Mon. Wea. Rev.*, **141**, 166–181, https://doi.org/10.1175/MWR-D-12-00176.1.

Ullrich, P. A., and C. M. Zarzycki, 2017: TempestExtremes: A framework for scale-insensitive pointwise feature tracking on unstructured grids. *Geosci. Model Dev.*, **10**, 1069–1090, https://doi.org/10.5194/gmd-10-1069-2017.

——, ——, E. E. McClenny, M. C. Pinheiro, A. M. Stansfield, and K. A. Reed, 2021: Tempestextremes v2.1: A community framework for feature detection, tracking, and analysis in large datasets. *Geosci. Model Dev.*, **14**, 5023–5048, https://doi.org/10.5194/gmd-14-5023-2021.

Vavrus, S., J. E. Walsh, W. L. Chapman, and D. Portis, 2006: The behavior of extreme cold air outbreaks under greenhouse warming. *Int. J. Climatol.*, **26**, 1133–1147, https://doi.org/10.1002/joc.1301.

Walsh, J. E., A. S. Phillips, D. H. Portis, and W. L. Chapman, 2001: Extreme cold outbreaks in the United States and Europe, 1948–99. *J. Climate*, **14**, 2642–2658, https://doi.org/10.1175/1520-0442(2001)014%3C2642:ECOITU%3E2.0.CO;2.

Westby, R. M., Y.-Y. Lee, and R. X. Black, 2013: Anomalous temperature regimes during the cool season: Long-term trends, low-frequency mode modulation, and representation in CMIP5 simulations. *J. Climate*, **26**, 9061–9076, https://doi.org/10.1175/JCLI-D-13-00003.1.

Wexler, H., 1936: Cooling in the lower atmosphere and the structure of polar continental air. *Mon. Wea. Rev.*, **64**, 122–136, https://doi.org/10.1175/1520-0493(1936)64%3C122:CITLAA%3E2.0.CO;2.

You, Y., and M. Ting, 2021: Observed trends in the south Asian monsoon low-pressure systems and rainfall extremes since the late 1970s. *Geophys. Res. Lett.*, **48**, e2021GL092378, https://doi.org/10.1029/2021GL092378.

Zhou, Y., T. A. O'Brien, P. A. Ullrich, W. D. Collins, C. M. Patricola, and A. M. Rhoades, 2021: Uncertainties in atmospheric river lifecycles by detection algorithms: Climatology and variability. *J. Geophys. Res. Atmos.*, **126**, e2020JD033711, https://doi.org/10.1029/2020JD033711.